EPJ manuscript No.
(will be inserted by the editor)

Resonance phenomena: from compound nucleus decay to proton radioactivity

R. J. Charity

Department of Chemistry, Washington University, St. Louis, Mo 63130, USA

Received: date / Revised version: date

Abstract. The role of resonances in exotic nuclei is investigated. This encompasses one and two nucleon emitters for ground-state nuclei beyond the drip lines to compound nuclei formed at higher excitation energies which, in some cases, can decay to produce these ground-state emitters. The role of barrier penetration and configuration mixing are both considered in explaining the long lifetimes observed in narrow resonances. Finally, two experimental techniques for studying exotic resonances are presented.

PACS. PACS-key discribing text of that key – PACS-key discribing text of that key

1 Introduction

Resonances are an essential ingredient for understanding nuclear phenomena both for the stable and more exotic nuclei. However as one approaches either the proton or neutron drip line, even the low-lying excited states of exotic nuclei are in the continuum, i.e., unbound to particle decay and thus are resonances. Eventually beyond the drip lines, even the ground states are themselves resonances. Clearly resonances have an especially important role for exotic nuclei.

We will start our exploration of resonances with some very simple ideas which illustrate some basic features of this phenomena and then gradually add more complexity associated with real nuclear resonances. In addition, we will consider many different types of resonances, for examples those with strong single-particle character, those in the region of overlapping resonances where configuration mixing is extreme, and those with three-body exit channels. These illustrate the diversity of current resonance studies and the continued interest in the field.

2 Basic Resonance Properties

2.1 One-Dimensional single-particle model

Many of the properties of resonances and their relevance for exotic nuclei can be illustrated by a simple one-dimensional single-particle model. By single-particle one means that each nucleon moves in an average potential generated by its interactions with the other nucleons. Otherwise, all other aspects of their interactions are ignored. For further simplicity we also assumed that these 1-d nuclei are composed of just one type of nucleon.

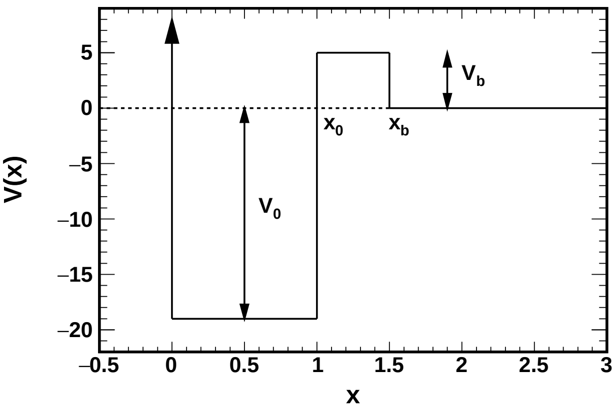

Fig. 1. Simplistic one-dimensional potential used in this work.

Once the mean field is defined, the Schrödinger equation can be solved to obtain the single-particle energy levels, i.e. the quantum energy states of nucleons within the nucleus. For our purposes we start with the very simple mean field displayed in Fig. 1. Note three important features of this mean field.

1. A potential well of depth V_0.
2. A barrier of height V_b separating the well from the continuum.
3. A continuum, i.e., the potential remains at zero out to $x = \infty$.

For simplicity we have assumed both a square well and a square barrier and, in addition, the potential goes to infinity at x=0 so as to only consider positive x values. The exact shape of the potential is not important in what follows, just the presence of these three features.

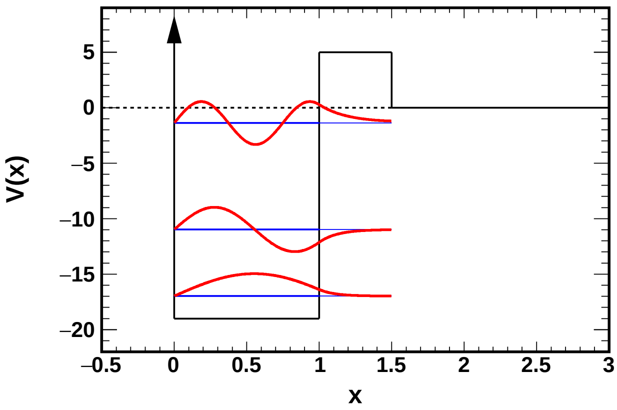

Fig. 2. Single-particle bound states obtained from the simple potential of Fig. 1. Bound state energies are indicated by the horizontal lines (blue) and the corresponding wavefunctions (red) are plotted relative to these lines.

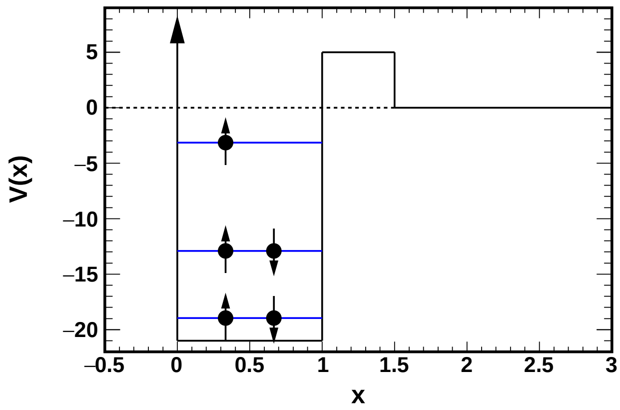

Fig. 3. The ground state of the A=5 nucleus in this simple 1-d single-particle model.

With this simple potential, one can easily solve the Schrödinger equation for bound-states ($E < 0$). In the region $x < x_0$, the solution is

$$\psi(x) = \mathcal{A}\sin(k_0 x) + \mathcal{B}\cos(k_0 x) \tag{1}$$
$$= \mathcal{A}\sin(k_0 x), \tag{2}$$

where $\mathcal{A}$ and $\mathcal{B}$ are integration constants and $k_0 = \sqrt{2m(E+V_0)}/\hbar$ where m is the nucleon mass. The second term must drop out ($\mathcal{B}$=0) as $\psi(0) = 0$ because $V(0) = \infty$. In the continuum region ($x > x_b$)

$$\psi(x) = \mathcal{E}\exp(\kappa_\infty x) + \mathcal{F}\exp(-\kappa_\infty x) \tag{3}$$
$$= \mathcal{F}\exp(-\kappa_\infty x) \tag{4}$$

where $\kappa_\infty = \sqrt{2m|E|}/\hbar$. In this case the first term must drop out ($\mathcal{E}$=0) in order for the wave function to be localized and normalizable. In the barrier region ($x_0 < x < x_b$),

$$\psi(x) = \mathcal{C}\exp(\kappa_b x) + \mathcal{D}\exp(-\kappa_b x), \tag{5}$$

where $\kappa_b = \sqrt{2m(V_b - E)}/\hbar$. Only at discreet energies E can one find values of $\mathcal{C}$, $\mathcal{D}$, and $\mathcal{F}$ (as functions of $\mathcal{A}$) such that the value of ψ and its derivative are continuous at both $x = x_0$ and $x = x_b$. Figure 2 shows the three bound eigenstates and their wavefunctions for the potential of Fig. 1. The ground state of the 1-d A=5 nucleus, is obtained by filling up these levels with nucleons with the lowest possible total energy as in Fig. 3. As we are dealing with Fermions, only two nucleons per level are allowed (spin up and spin down). In this case we have two completely filled levels and one partially filled (valence) level which is weakly bound. Particle-bound excited states of this nucleus can then be obtained by promoting one of the more deeper-bound nucleons to this valence level.

Now imagine we are at liberty to modify the potential by decreasing the depth of the well (V_0). The result of such a modification is to push all the single-particle levels up in energy. If we keep decreasing the depth of the well, eventually our least-bound valence level will cross zero energy. So what does our formally bound state turn into when its crosses zero energy? What kind of states is it?

To answer these questions, consider the classical case of a nucleon with positive energy ($0 < E < V_b$) located inside of the barrier. It will of course bounce backwards and forwards between $x = 0$ and $x = x_0$ forever. Now allow quantum tunneling to a occur. Each time the nucleon attacks the barrier, there is a probability it will tunnel through and escape from the system. Thus, the probability that the particle stays behind the barrier is reduced by a constant scaling factor for each attack and therefore this probability decreases exponentially with time.

Gamov first considered exponentially-decaying solutions of the Schrödinger equation. As we are interested in a time-dependent solution we must start with the time-dependent Schrödinger equation

$$i\hbar\frac{\partial}{\partial t}\Psi(x,t) = \left[\frac{-\hbar^2}{2m}\frac{\partial}{\partial x^2} + V(r)\right]\Psi(x,t). \tag{6}$$

Let us look for a solution where Ψ is separable in the time and position coordinates, i.e.,

$$\Psi(x,t) = \exp\left(\frac{-iEt}{\hbar}\right)\psi(x). \tag{7}$$

If we use a complex energy $E = E_r - i\Gamma/2$, then the modulus squared of the wave function,

$$|\Psi(x,t)|^2 = \exp\left(\frac{-\Gamma t}{\hbar}\right)|\psi(x)|^2, \tag{8}$$

decays exponentially. In general, exponentially-decaying (or increasing) solutions can be obtained by solving the time-independent Schrödinger equation with a complex energy. We still have to choose the boundary condition at large x to solve the problem. As there is no flux coming into the potential, then in the region $x > x_b$, the solution

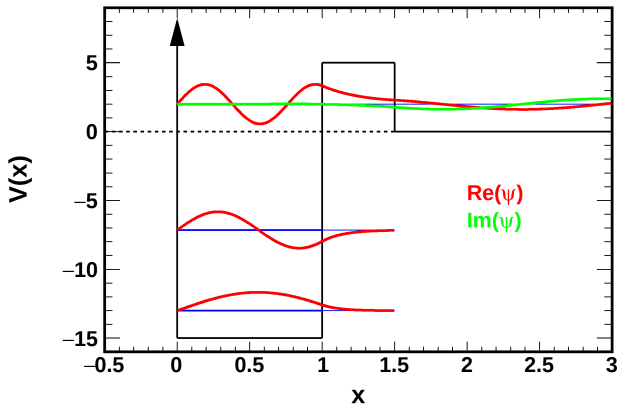

Fig. 4. Bound and exponentially decaying states obtained for the potential of Fig. 1, but with a somewhat shallower well. The exponentially decaying wavefunction has both real and imaginary components, while the bound-state wavefunctions are only real.

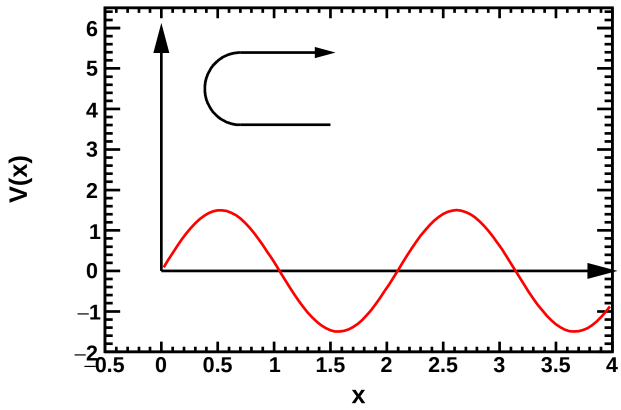

Fig. 5. Scattering wave function (red) obtained for the simple case where the potential well and barrier of Fig. 1 are missing. Here the potential (black) is uniform above x >0. The classical motion is indicated by the arrow showing a reflection at the x=0 wall.

must be just an outgoing wave:

$$\Psi(x,t) = \mathcal{H} \exp\left[i\left(\frac{-Et}{\hbar} + k_\infty x\right)\right], \tag{9}$$

$$k_\infty = \sqrt{2mE}/\hbar. \tag{10}$$

Otherwise, the solutions for $x < x_0$ and $x_0 < x < x_b$ are again given by Eqs. (2) and (5). By again demanding the wavefunction and its derivation are continuous at both $x = x_0$ and $x = x_b$, we now find solutions only at discrete complex energies. Such states are single-particle resonances and if a nucleon is placed in such a single-particle state it produces a nuclear resonance in this simplistic model. Figure 4 shows the bound and resonance solutions for a potential which is somewhat shallower than that in Figs. 1 and 2. Notice that the third bound single-particle state in Fig. 2 that turned into a resonance in Fig. 4 has similar character in the two figures with two nodes inside of the potential well. As the state has a finite lifetime $\Delta t = \hbar/\Gamma$, then it has an energy uncertainty ΔE_r. By Heisenberg's uncertainty principle

$$\Delta E_r \Delta t \sim \hbar \tag{11}$$

and thus ΔE_r is of order Γ.

Historically, resonances have a stronger relationship with scattering phenomenon. Indeed in our simple model, resonances can also be probed by scattering as well. Consider first the very simple case of scattering where the potential well and barrier are both missing as illustrated in Fig. 5.

The solution to the time-independent Schrödinger equation with positive energy is just a single sine curve, i.e.,

$$\psi(x) = \mathcal{A} \sin(k_\infty x) \tag{12}$$

$$= \frac{\mathcal{A}}{2i}\left[\exp(ik_\infty x) - \exp(-ik_\infty x)\right]. \tag{13}$$

This solution can be considered as a standing wave due to the interference of ingoing and outgoing waves. These become obvious in the expansion of the sine function into exponentials in Eq. (13). The $\exp(-ik_\infty x)$ term is the incoming wave while the $\exp(ik_\infty x)$ term in the outgoing wave. Classically as indicated by the arrow in Fig. 5, a particle coming in from large x gets reflected off the $V = \infty$ boundary at $x = 0$ and goes back out again.

Now let us consider scattering when the potential well and barrier of Fig. 4 are included. Classically if the scattering energy is less than the barrier ($E < V_b$), then an incoming particle is reflected by the barrier and never enters the potential well. However, with quantum tunneling, there will be a non-zero probability of it being in the well. Let us define this probability as

$$P_{well} = \int_0^{x_0} |\psi(x)|^2 \, dx. \tag{14}$$

In addition, the wavefunction in the exterior region ($x > x_b$) will no longer be just a sine wave, but a cosine wave solution can also contribute, i.e..

$$\psi(x) = \mathcal{A}\sin(k_\infty x) + \mathcal{B}\cos(k_\infty x) \tag{15}$$

$$= \sqrt{\mathcal{A}^2 + \mathcal{B}^2}\sin(k_\infty x + \delta) \tag{16}$$

$$= \frac{\sqrt{\mathcal{A}^2 + \mathcal{B}^2}}{2i}\exp(-\delta)\left[\exp(ik_\infty x + 2\delta) - \exp(-ik_\infty x)\right] \tag{17}$$

In Eq. (16), this is also expressed in terms of a phase shift $\delta = \text{atan}(\mathcal{B}/\mathcal{A})$ relative to the standing wave solution of Eq. (13) without the potential well and barrier. Notice from Eq. (17) this leads to a phase shift of 2δ between the incoming and outgoing waves.

The quantity P_{well} and the phase shift δ for the same potential as in Fig. 4 are shown in Fig. 6 as a function of scattering energy. In Fig. 6(a), the relative probability of getting a particle inside of the potential well has a strong

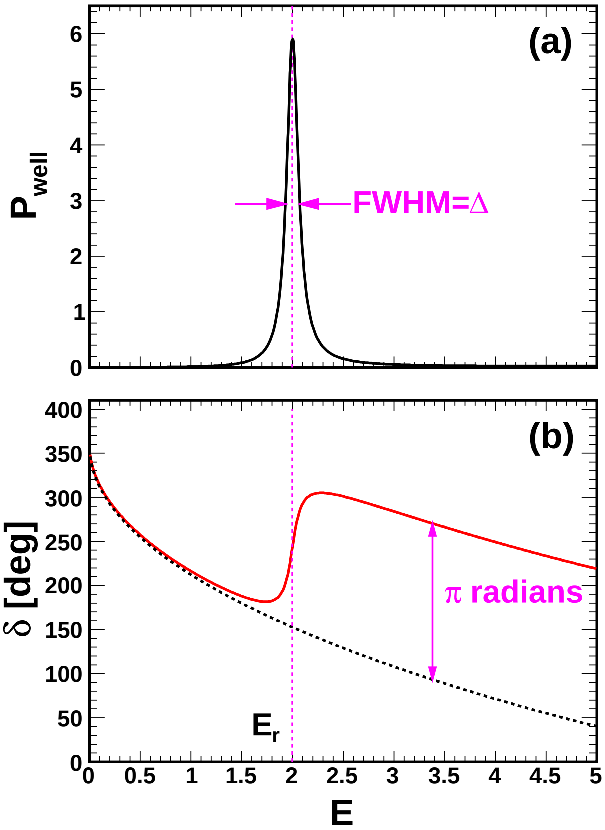

Fig. 6. Energy dependence for scattering. (a) shows the relative probability that the nucleon is inside of the well while (b) shows the phase shift. At the resonance energy, the phase shift shows a sharp jump of π radians.

resonant peak. For narrow peaks, the centroid of such a peak has the same value as E_r, the real energy obtained in the exponentially-decaying solution (Fig. 4). The peak shape is given by a Breit-Wigner form:

$$P_{well} \propto \frac{\Gamma^2}{(E-E_r)^2 + (\Gamma/2)^2} \tag{18}$$

where here Γ is the full width at half maximum (FWHM) of the peak. Again in the limit of a narrow resonance, the value of Γ obtained from the FWHM is the same as that obtain for the exponentially-decaying solution in Eq. (8).

The phase shift in Fig. 6(b) shows a sudden change of magnitude π radians relative to the more slowly decreasing background phase. This is a defining feature of all narrow resonances. As the resonance becomes very wide it can be difficult to differentiate the phase shift of the resonance from that associated with the slowly varying background.

Our simple model has documented three important features of resonances

1. If a resonance state of the nucleus is created, it will decay with a exponential time distribution with a lifetime of $\hbar/\Gamma$.
2. The resonance can also be probed in scattering experiments, where the scattering cross section (which is related to P_{well}) peaks at the resonance energy with a FWHM of Γ.
3. As the energy is scanned across a resonance, the phase shift in the exterior region of the scattering wave function undergoes a jump of π radians relative the more slowly varying background phase.

There three feature are quite general and apply for more complicated resonances which are not adequately described by our simple 1-d single-particle model.

2.2 Three-dimensional single-particle model

Let us now make a first step towards a more realistic model by considering three-dimensions. Consider a wavefunction corresponding to a plane wave traveling along the z axis. In polar coordinates, the partial wave expansion of this plane wave is

$$\psi(z) = \exp(ik_\infty z). \tag{19}$$

$$= \sum_{\ell=0}^{\infty} (2\ell+1) i^l j_l(k_\infty r) P_\ell(\cos\theta), \tag{20}$$

where P_ℓ are Legendre polynomials and the spherical Bessel functions have the asymptotic form

$$j_\ell(k_\infty r) \rightarrow \frac{\sin(k_\infty r - \ell\frac{\pi}{2})}{kr} \text{for } r \rightarrow \infty \tag{21}$$

and thus at large r, Eq. (20) becomes

$$\psi \rightarrow \sum_{\ell=0}^{\infty} \frac{2\ell+1}{2ik_\infty r} P_\ell(\cos\theta) \left[\exp(ik_\infty r) - (-1)^\ell \exp(-ik_\infty r)\right] \tag{22}$$

which is just the sum of ingoing $[\exp(-ik_\infty r)]$ and outgoing $[\exp(ik_\infty r)]$ spherical waves. Now remember this expansion is just for a plane wave with no scattering potential. If we add a spherical symmetric potential, we can now write the solution as

$$\psi \rightarrow \sum_{\ell=0}^{\infty} \frac{2\ell+1}{2ik_\infty r} P_\ell(\cos\theta) \times \left[S_{\ell,j} \exp(ik_\infty r) - (-1)^\ell \exp(-ik_\infty r)\right] \tag{23}$$

where the outgoing wave is modified by the factor $S_{\ell,j}$ called the S-matrix. The S-matrix depends on the orbital angular and the total angular momentum which is comprised of ℓ and the spin of the scattered nucleon. We will ignore any coupling to the target spin in this work. For processes like we investigated in the 1-d model (Sec. 2.1), there is no absorption, so the modulus of $S_{\ell,j}$ is unity and is just related to the phase shift as in Eq. (17) and

$$S_{\ell,j} = \exp(2i\delta_{\ell,j}). \tag{24}$$

If there is some absorption of the incoming flux then $|S|^2 < 1$. Such absorption can be incorporated theoretically by use of an imaginary component to the potential.

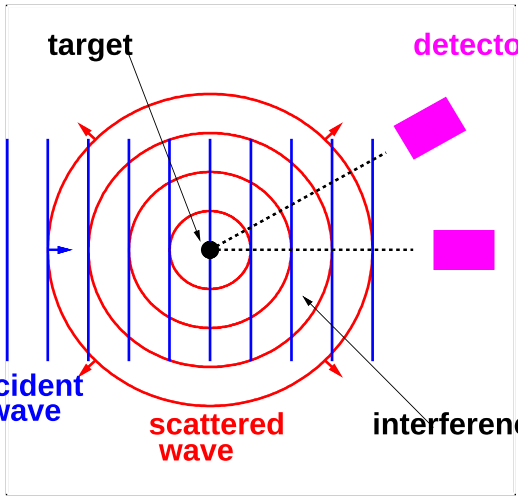

Fig. 7. Schematic illustrating the scattering wave function components.

The final asymptotic wavefunction with a scattering potential can also be written as

$$\psi \to \exp(ik_\infty z)+ \tag{25}$$

$$\sum_{\ell=0}^{\infty} \frac{2\ell+1}{2ik_\infty r}(S_{\ell,j}-1)\exp(ik_\infty r)P_\ell(\cos\theta), \tag{26}$$

i.e, the incidence plane wave plus a sum of scattered spherical waves as shown schematically in Fig. 7. In calculating the angular distribution of the scattered particle one must also consider the interference between these two components.

Note that at a resonance, the probably that a particle enters the potential well is large as demonstrated in Sec. 2.1. When such particles eventually tunnel back out they are emitted in all directions. Therefore there are two ways to observed such resonances in experiments.

1. Observe their scattering to finite angle away from the beam axis. The detected particle must have the same energy as the beam (elastic scattering) to differentiate this from other processes.
2. Observe the loss of particles traveling in the beam direction. The magnitude of this loss is related to the total cross (σ_{tot}). This total cross is only useful for neutron scattering, as it is infinite for charge-particle scattering due to the long-range nature of the Coulomb potential.

As an example of resonances in real nuclei, we start with a non-exotic case and focus on the levels of ^{13}C. Its level scheme is shown in Fig. 8 and the lowest three excited states are particle stable and decay to the ground state by γ-ray emission. In the single-particle model, these levels

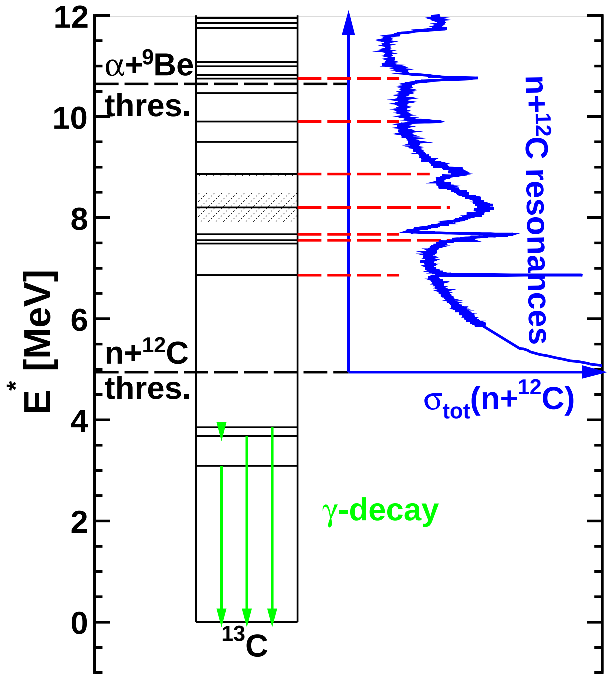

Fig. 8. The level scheme of ^{13}C and the total n+^{12}C cross section [16] showing the correspondence between the n+^{12}C resonance peaks and particle unstable levels of ^{13}C.

would be obtained from configurations where nucleons are in bound single-particle levels only. The neutron separation energy for ^{13}C is 4.94 MeV and this is the threshold for breakup into the n+^{12}C channel. All the ^{13}C levels above this energy are resonances. The next highest separation energy is for α particles at 10.64 MeV, so between between 4.94 and 10.64 MeV, the only open particle decay mode is neutron emission. Above 10.64 MeV, neutron and α decay are possible and at 17.53 MeV, proton decay channels are open as well.

In Fig. 8, the total neutron cross section on ^{12}C as a function of neutron energy from Ref. [16] is also shown. This cross sections has many peaks or resonances, both narrow and wide, and one can see that these correspond directly to excited states in ^{13}C. Note, not all excited states above the neutron threshold have visible resonances associated with them. Such peaks do not have strong single-particle structure. The α+^{9}Be scattering data also shows resonance peaks, but these correspond to highly lying level above the the α separation energy of 10.64 MeV.

2.3 Symmetry Dependence of mean field potential

So far we have largely ignored the fact that nuclei are composed of two types of nucleons. In this section we will discuss a consequence of this for resonances. In Sec. 2.1 we discussed what happens when we modify the depth of the potential well in Fig. 1. This well is produced by the mean potential that a nucleon feels from all the other nucleons in the nucleus. It turns out we can indeed modify the depth of this well quite easily. Given that the proton-neutron interaction is stronger than the proton-proton or the neutron-neutron interactions, then if we keep the same number of nucleons but change the ratio of protons to neutrons, the mean fields felt by the two nucleon types will change. Their depths have been found to have the form

$$V_0 = V' + v_{sym}\frac{N-Z}{A} \text{ protons} \tag{27}$$

$$= V' - v_{sym}\frac{N-Z}{A} \text{ neutrons.} \tag{28}$$

where V' and v_{sym} are constants. Compared to $N \sim Z$ nuclei, for neutron-rich systems where the symmetry parameter $(N-Z)/A$ is large, protons are surrounded by more neutrons and thus the depth of their mean field is larger. On the other hand, neutrons have less protons surrounding them and therefore the depth of their mean field in smaller.

This symmetry dependence of the mean field contributes about 50% of the symmetry energy in the semi-empirical mass formula used to fit and predict the binding energies of nuclei

$$E_{binding}(Z,A) = a_{vol}A - a_{sur}A^{2/3} - a_{Coul}\frac{Z^2}{A^{1/3}} - a_{asy}\frac{(N-Z)^2}{A}. \tag{29}$$

The terms here are called the volume, surface, Coulomb, and symmetry energies and a_i coefficients are fit to experimental data. Remember protons are more bound if there are more neutrons around while neutrons are more bound if there are more protons around. The symmetry term includes both of these two effects plus a kinetic contribution. As a compromise, the symmetry term gives the strongest binding for equal numbers of protons and neutrons.

To illustrate the importance of the symmetry force for the single-particle energies, Fig. 9 shows a schematic of the proton and neutron single-particle levels in fluorine isotopes. As ^{19}F is the only stable fluorine isotope, its neutron and proton separation energies must be similar. By moving towards the proton drip line (decreasing the number of neutrons) the proton mean field become shallower while the neutron mean field becomes deeper. At ^{18}F this change in mean fields has made a significantly difference in the two separation energies and in this case, the difference is large enough that energetically the weak interaction can turn a valence proton into a neutron and thus this isotope is β unstable.

At ^{17}F, the valence proton level (highest occupied level) is just below the continuum (zero energy) and at ^{16}F, this level is now in the continuum. Thus by decreasing the number of neutrons we have made a proton resonance. Of course if we decreased the number of protons, we could make a neutron resonance instead.

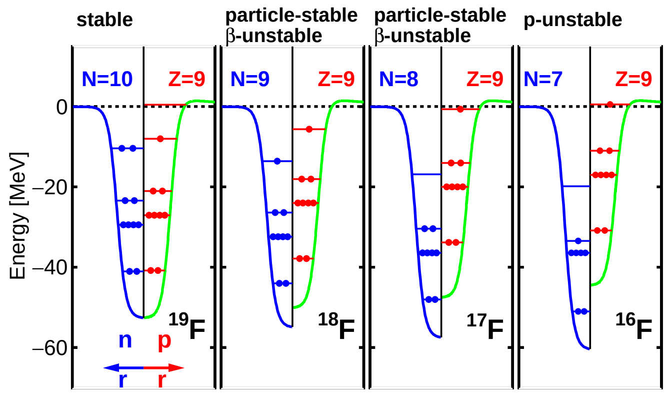

Fig. 9. Schematic showing the evolution of neutron and proton single-particle levels with mass number A for fluorine isotopes. For each isotope, neutron (proton) single-particle levels and the mean field as a function of radius r are shown on the left (right)

3 Beyond the Single-Particle Model

In the single-particle picture, nuclear resonances are created by placing one or more of the nucleons in single-particle resonance states. To produce a single-particle resonance we need a barrier to constrain the nucleon close to the nucleus for a significant time. Thus in this simple picture, ℓ=0 neutrons should not be able to produce resonances as they have no Coulomb and no centrifugal barrier. Therefore for neutrons incident on spin-zero target nuclei (even Z and even N) we should not see any J=1/2$^+$ resonances (total angular momentum just equal to the neutron spin as ℓ=0). However such resonances are quite common.

Also even if there is a barrier, resonances are not possible at high excitations energies in this model as the energy of the nucleon must be less that the barrier height for it to be temporarily trapped. However resonances do not disappear at higher excitation energies. Clearly this points a major failure of the single-particle model. While some low-lying states do have strong single-particle character, many other states do not, especially at high excitation energies.

How does one create long-lived nuclear states when there is no barrier or the barrier is too low to trap the incoming nucleon? The answer lies in the fact that real nuclear states are admixtures of these single-particle configurations. For some nuclear states, one particular or a couple of a single-particle configurations dominate and these are said to have strong single-particle character. Other states are admixtures of many single-particle configurations. Consider a nucleon scattering; when the nucleon and target start to touch, this initial single-particle configuration can couple to other more complex configurations which are bound or at least constrained by a barrier. The system can eventually recouples back to the original entrance channel configuration and the nucleon can then escape from the target. Configuration mixing thus provides a mechanism for the incidence nucleon to be held in the target thus giving the resonance a lifetime.

In addition to allowing for a finite lifetime, configuration mixing allows for a resonance to have multiple decay paths if such channels have components in the resonance's wavefunction. If a resonance C couples to open channels $a+b$ and $c+d$, then we can observed the following scattering reactions with their associated cross sections:

$$a+b \rightarrow C \rightarrow a+b, \quad \sigma = G\frac{\Gamma_{a+b}^2}{(E-E_r^{a+b})^2+(\Gamma_{tot}/2)^2} \tag{30}$$

$$a+b \rightarrow C \rightarrow d+e, \quad \sigma = G\frac{\Gamma_{a+b}\Gamma_{d+e}}{(E-E_r^{a+b})^2+(\Gamma_{tot}/2)^2} \tag{31}$$

$$d+e \rightarrow C \rightarrow a+b, \quad \sigma = G\frac{\Gamma_{d+e}\Gamma_{a+b}}{(E-E_r^{d+e})^2+(\Gamma_{tot}/2)^2} \tag{32}$$

$$d+e \rightarrow C \rightarrow d+e, \quad \sigma = G\frac{\Gamma_{d+e}^2}{(E-E_r^{d+e})^2+(\Gamma_{tot}/2)^2} \tag{33}$$

Here $G = \pi/k_\infty^2(2J_C+1)/(2J_1+1)/(2J_2+1)$ and J_C is the spin of the resonance, while J_1 and J_2 are the spins of the two particle in the entrance channels. E_r^{a+b} and E_r^{d+e} are the resonance energies above the appropriate thresholds. For example in reaction (30), J_1 and J_2 are just the spins of particles a and b. Each open decay channel has a partial decay width associated with it. In the above example, these are Γ_{a+b} and Γ_{d+e} and the total decay width is of course the sum of these partial widths, i.e., $\Gamma_{tot} = \Gamma_{a+b}+\Gamma_{d+e}$. The cross section of Eqs. (30) and (31) should be interpreted as follows: the total cross section for the formation of the resonance is

$$\sigma = G\frac{\Gamma_{a+b}\Gamma_{tot}}{(E-E_r^{a+b})^2+(\Gamma_{tot}/2)^2} \tag{34}$$

Once the resonance is created, it has a probability or branching ratio of $\Gamma_{a+b}/\Gamma_{tot}$ for decay to the $a+b$ channel and $\Gamma_{d+e}/\Gamma_{tot}$ for decay to the $d+e$ channel. These branching ratios apply no matter how the resonances was created.

In R-matrix theory [11], the partial decay width for a channel λ is

$$\Gamma_\lambda = 2k_\infty R P_\ell \Theta_\lambda^2 \gamma_\lambda^2 \tag{35}$$

where R is the channel radius, P_ℓ is the angular-momentum-dependent barrier penetration probability, $\gamma_\lambda^2 = 3\hbar^2/2MR^2$ is the reduced single-particle width, and Θ_λ^2 is the fractional reduced width. For a pure single-particle state, $\Theta_\lambda^2 = 1$, and the final width is determined from the barrier penetration probability. For states of mixed configurations, $\Theta_\lambda^2 < 1$. Nuclear resonances with energies above the barrier such that $P_\ell \rightarrow 1$ can be narrow if Θ_λ^2 is small (large mixing).

4 Experimental techniques to measure exotic resonances

Resonances can be probed experimentally by a number of techniques. In this section we will discuss just two examples, one that involves scattering and one that looks directly at the resonance decay products.

4.1 Resonance elastic scattering

There is a long history of probing resonances with stable targets using elastic scattering. By elastic one means that the projectile is just deflected without losing any energy. At low energies, elastic scattering is dominated by resonance scattering. Using beams of neutrons, protons, or α particles one measures the cross section for these particles to be scattered at one or more angles and then modifies the beam energy in small increments to scan an energy region and map out the resonance peaks. Such a technique does not work for exotic nuclei near and beyond the drip lines as no stable target nuclei exist. The appropriate target isotopes have short half-lives making the fabrication of physical targets impossible.

The solution to problem is to turn the reaction around and use exotic beams rather than exotic targets. Isotopes with half-lives greater than 1 ms can readily be made into beams. For example, instead of shooting protons on an exotic target, we can shoot an exotic beam on hydrogen target nuclei. Although pure hydrogen targets are sometimes used, they are not always necessary, one can often use a polyethylene [$(C_2H_4)_n$] or methane (CH_4) targets and from measuring appropriate quantities separate out products produced with the hydrogen and carbon components of these targets. This technique of turning the reaction around, called reverse kinematics, does not work for neutrons of course, one cannot make a neutron target. So elastic scattering in reverse kinematics can only be used to probes exotic proton or other charged-particle resonances.

Consider the schematic shown in Fig. 10 for measuring proton resonances in ^{14}F. The latter isotope is beyond the proton drip line so its ground state is a resonance as well as all its excited states. A ^{13}O radioactive beam is directed into a volume containing hydrogen or methane gas. The ^{13}O ground state has a 8.6 ms half life and is situated just inside the proton drip line. Interactions of the ^{13}O beam with the gas molecules cause the beam particles to slow down and the gas pressure and volume length are chosen so that the beam will stop within the gas volume. This all happens in a time scale significantly smaller than the liftime of 8.6 ms. While the ^{13}O fragments are slowing down, it is also possible for them to elastically scatter off the hydrogen nuclei in the gas molecules. If the hydrogen nuclei (protons) are scattered forward they are given high velocities. In the limit that the beam mass number A is large, the forward-going proton are recoiled to twice the velocity of the beam at the time of the collision. The large velocities and smaller charge on the protons means they can travel much further in the gas before stopping than the ^{13}O projectiles. Proton detectors are places at forward angle to intercept these protons are they leave the gas volume and measure their kinetic energy. In addition, the time from when the ^{13}O isotope entered the volume until the proton is detected is recorded. The latter is used to remove events with are not elastic or from interactions with the carbon nuclei if methane gas is used.

With knowledge of the stopping powers of ^{13}O ions and protons in the gas, one can determine a unique relation-

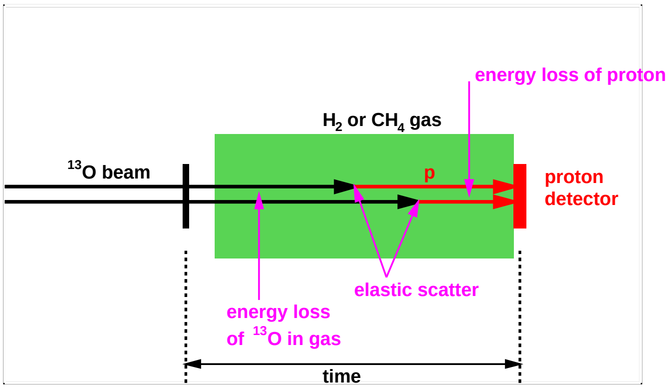

Fig. 10. Schematic showing the resonance elastic-scattering method with exotic beams.

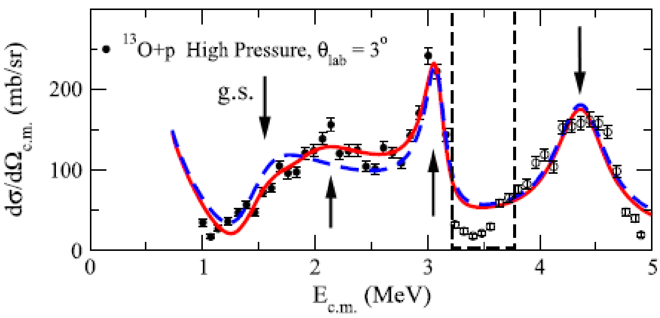

Fig. 11. Elastic scattering cross sections for p+^{13}O determined by Goldberg et al. [7] as a function of proton energy. Arrows show the location of fitted resonances in ^{14}F with the ground state (g.s.) resonance labeled.

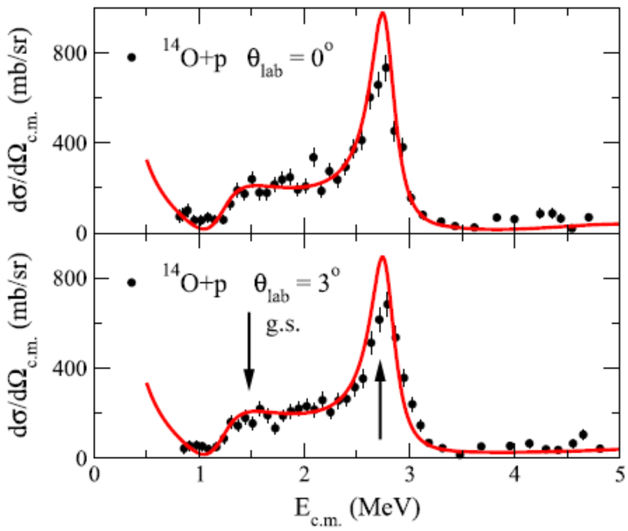

Fig. 12. Elastic scattering cross sections for p+^{14}O determined by Goldberg et al. [7]. as a function of proton energy.

ship between the detected proton energy and the location in the gas volume at which the elastic-scattering event occurred. From this one can determine the energy of the ^{13}O before the scattering event and the energy of the proton after this event. One can then plot the elastic scattering cross section as a function of ^{13}O energy or equivalent proton energy in normal kinematics and look for resonances. One advantage of this method is that an energy scan is done automatically, i.e. all energy below the beam energy are probed in one setting.

The elastically-scattered cross sections measured by Goldberg *et al.* [7] are shown in Fig. 11. The centroid of the resonance peaks, as obtained from fits to these data (curves), are indicated by the arrows. The two higher-energy resonance peaks are quite clear in this example, however the two lower-energy resonances overlap and are more difficult to extract. Figure 12 shows another example of resonance elastic scattering, this time for the neighboring reaction p+^{14}O making resonances in ^{15}F. In this case there are only two resonances, the ground-state which is not very pronounced and the much more pronounced first excited state.

Inverse-kinematic resonance elastic scattering has a role in mapping out the resonances in nuclei beyond the proton drip line. Look at Fig. 13 where a portion of the chart of nuclides for light systems is shown. The small (blue) arrows indicate the fluorine isotopes beyond the proton drip line which have been, or could be, accessed by this technique. Notice that it would not be possible to study ^{13}F by this method as it does not have a particle-stable (red) isotopes below it (^{12}O, $t_{1/2}$ ∼10^{-21} s) which lives long enough to be accelerated and used as a beam. There are certainly many other cases that cannot be accessed by this technique, but it is quite important for odd-Z nuclei like fluorine.

4.2 Invariant-mass spectroscopy

In the theory of relativity, the invariant mass of an object is just its rest mass. For a systems of objects, the invariant mass is just the total relativistic mass in their center-of-mass frame. Invariant-mass spectroscopy is used when all the decay products of a resonance are detected and identified. Histograms of their measured invariant mass will show peak associated with the resonance. The reaction by which the resonance is made is not so important, it could be elastic scattering, but more likely it involves transfer, knockout, or pickups reactions where the nucleons are added or removed from the projectile nucleus.

Rather than invariant mass, one often plots the total decay kinetic energy E_T which differs from the former by the sum of the rest masses of each of the decay products. For example, consider the kinematics for the two-body decay of ^{16}F to p+ ^{15}O shown schematically in Fig. 14. The center-of-mass velocity vector ($v_{c.m.}$ of the two decay products is of course just the velocity of the ^{16}F resonance [v_{lab}(^{16}F)] before it decayed. Subtracting this velocity from the measured velocity of both fragments [$v_{lab}(p)$ and v_{lab}(^{15}O)] gives us the velocities at which they were emitted by the decaying ^{16}F fragment (v_p and $v_{^{15}O}$). The total decay kinetic energy E_T can then be obtained from

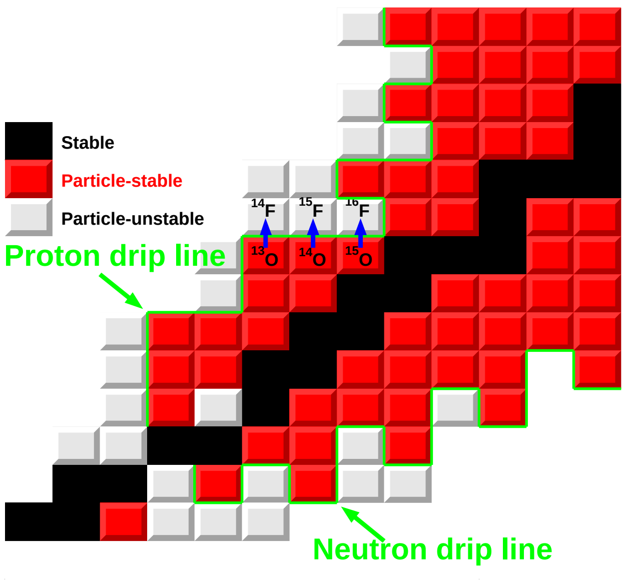

Fig. 13. The chart of nuclides in the region for the very light nuclei showing the drip lines, the stable, particle-stable, and particle-unstable nuclei. The small (blue) arrow indicate the fluorine isotopes beyond the proton drip line which can be accesses by inverse-kinematics resonance elastic-scattering.

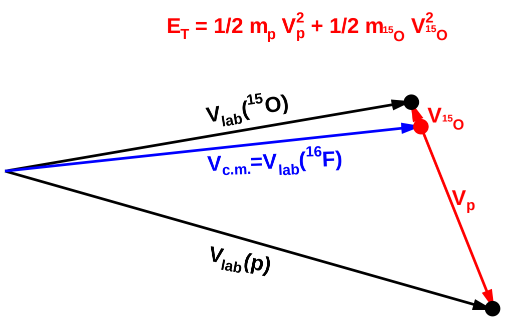

Fig. 14. Schematic showing the kinematics for the decay of a ^{16}F resonance into the p+^{15}O channel.

the kinetic energy of the two fragments in this center-of-mass frame.

To perform invariant-mass spectroscopy, one needs a detector array that covers the angular and energies ranges of the emitted decay products. In addition, the velocity vectors of all fragments need to be detected accurately. The latter is usually achieved with measurements of both the energies and angles of the decay products. The device I use extensively for this is the HiRA (High Resolution Array) detector [17]. A picture of this device in the configuration used for invariant-mass studies is shown in Fig. 15. The front elements of 14 telescopes are visible.

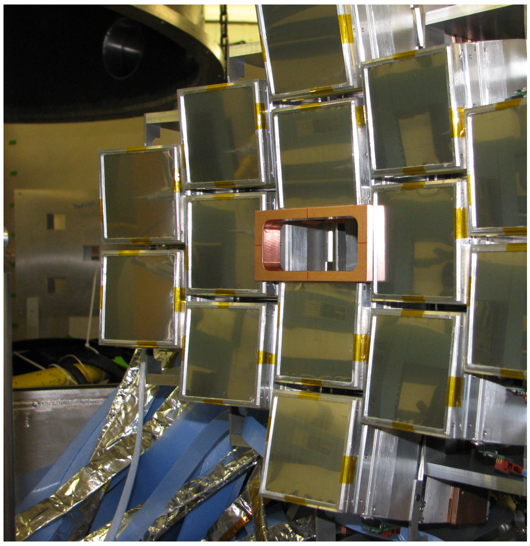

Fig. 15. An image of the HiRA detector array in its configuration used for invariant-mass spectroscopy

Each of these front elements is comprised of silicon strip detectors. There are 32 strips on the front and 32 strips on the back. The front and back strips are orientated perpendicular to each other. A particle passing through these silicon detectors will fire one strip on the front and one strip on the back which allows us to determine the scattering angle very accuracctely. Behind the silicon strip detectors are thick CsI scintillators which stop the incident particle. The light output of these scintillators is measured with photodiodes and gives information of the kinetic energy of the incident particle.

As an example, the decay-energy spectrum measured for the p+^{15}O channel of ^{16}F resonances is displayed in Fig. 16. It was obtained from events where a proton and a ^{15}O fragments were detected in coincidence following interactions of a ^{17}Ne beam upon a ^{9}Be target. Peripheral collisions can create ^{16}F resonances by knocking out a proton from the beam projectile. Resonance peaks for the ground and three excited states are observed, although the first-excited state is not that prominent.

The invariant-mass technique is used quite extensively in high-energy physics. For example, Fig. 17 shows the invariant-mass spectrum obtained from events with two high-energy γ rays measured from p-p collisions at CERN. The spectrum consists of a small bump on a smoothly falling background. The lower panel shows the results when a smooth background is subtracted revealing a peak at 125 GeV which has been assigned to the Higgs Boson [1]. The Higgs boson also has many other possible decay channels, but the invariant-mass should be the same in all these channels as it is just a measure of the Higgs mass.

5 Three-body Resonances

Up until now we have only considered resonances which couple to two-body exit and entrance channels. However

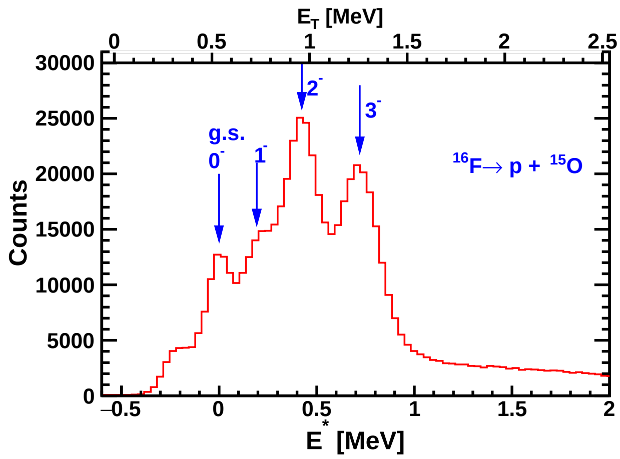

Fig. 16. Invariant-mass technique for ^{16}F resonances obtained from detected p+^{15}O events. Axes for both the decay energy E_T and the excitation energy E^* are shown.

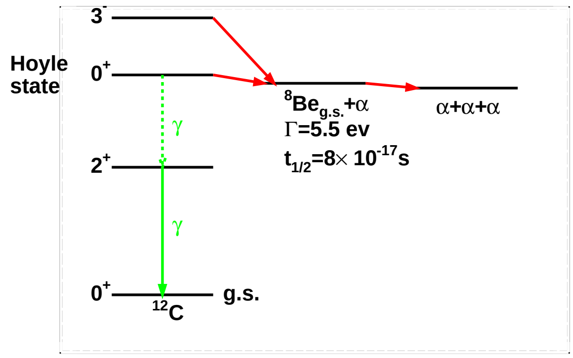

Fig. 18. Level Scheme of ^{12}C showing the Hoyle state and its decay paths.

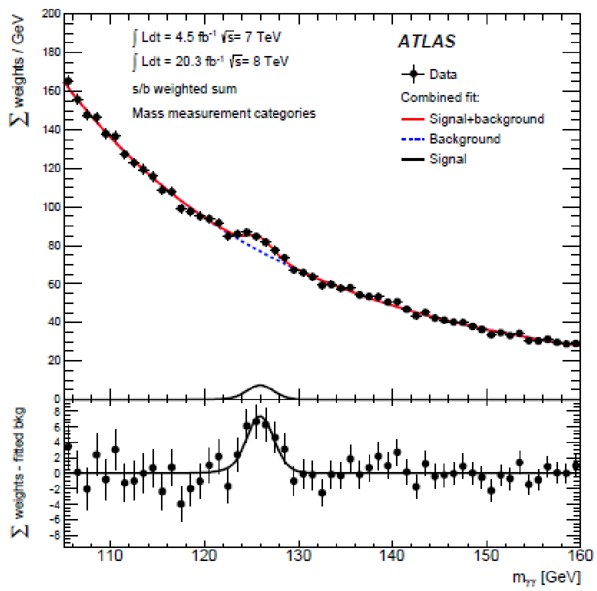

Fig. 17. (top) Invariant-mass distribution for γ-γ pairs form p+p collisions at CERN. (bottom) The same spectrum after a smooth background spectrum has been subtracted revealing a peak at 126 GeV corresponding to the Higgs Boson. (Figure from Ref. [1]).

resonances can have three or more particles in these channels. Experimentally three-particle scattering is not something that can be accomplished in the laboratory and we rely on other reaction mechanisms to create these resonances and the multi-particle exit channel can then be observed. Invariant-mass spectroscopy can then easily be extended to such resonances as long as all the decay products are detected.

Three-body resonances are usually described as one of two kinds:

1. Prompt or "true" three-body decay where all three final fragments are created at the same instance.
2. Sequential where the decay is really two sequences of two-body decay. Such a decay should be considered as a two-body decay but where one of the final products of the first decay is a two-body resonance which then subsequently decays.

The sequential mechanism is distinct from prompt decay as long as the intermediate resonance is long-lived so that there is no interaction between the products produced in the two steps.

5.1 Sequential decay

An example of a sequential three-body decay is the second excited state of ^{12}C, the so-called Hoyle state, named after Fred Hoyle who predicted its existence was necessary in order to make carbon and heavier elements in stars. The low-lying level scheme for ^{12}C is shown in Fig. 18. The Hoyle state is the second J^π=0$^+$ state in ^{12}C at E^*=7.65 MeV. This state decays into an α particle and the ground-state of ^{8}Be. The latter is itself a resonance and decays into two α particles. So the Hoyle states decays by two steps of binary breakup to produce three α particles. The ^{8}Be intermediate resonance has a half life of 8$\times$10^{-17} s and in one half life, the first emitted α particle moves 370000 fm away from the ^{8}Be resonance. This is a relatively huge separation, compared to the radius of ^{12}C ($\sim$3 fm). Therefore there are no interactions between the first α particle and those emitted from the decay of the ^{8}Be intermediate.

Astrophysically, the creation of ^{12}C occurs in the reverse order. Two α particles coalesce to make a ^{8}Be resonance. If another α particle comes along at the right energy before this ^{8}Be resonance decays, then the Hoyle state can be made. In most cases, the Hoyle state sequentially decays back again into three α particles. However the Hoyle state has a very small γ-decay branch to the first excited state of ^{12}C. The latter decays by γ emission to the ground state.

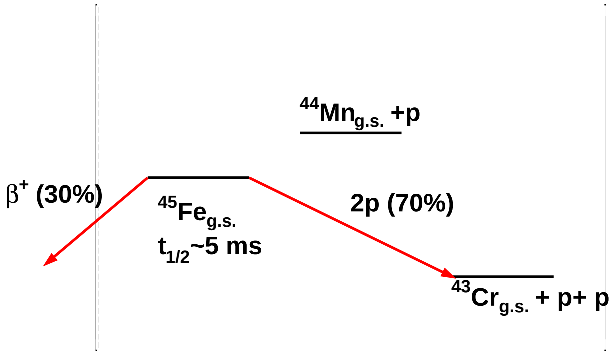

Fig. 19. Schematic showing the levels important for the decay of ^{45}Fe.

5.2 Two-Nucleon Decay

The possibility of promptly emitting of two nucleons from the ground state of exotic nuclei was first considered by Goldansky in 1960. Goldansky looked for isotopes where single-nucleon emission was not energetically possible, but two-nucleon emission was allowed. As an example, consider the two-proton decay of ^{45}Fe which is located just beyond the proton drip line. As shown in Fig. 19, single-proton emission from the ground state of ^{45}Fe to the ground state of ^{44}Mn is not possible energetically. However, two-proton decay to the ground state of ^{43}Cr is possible. Therefore the only open particle-decay mode is a prompt two-proton decay. This decay was observed in an optical time projection chamber (TPC) where the ionization tracks of the decay products in gas are visualized. Figure 20 shows an example of such a track measured by Miernik *et al.* [13]. The two-proton decay rate is slow enough in this nucleus that β^+ decay has time to compete. However, the two-proton decay branch still dominates and it branching ratio is ~70%.

The occurrence of ground-state two-proton emitters in the prescription of Goldansky is a consequence of pairing interaction, making even-Z nuclei more bound relative to odd-Z neighbors. Thus situations like that depicted in Fig. 19 where the one-proton channels is inaccessible while the two-proton is available are only found for even-Z ground-states beyond the proton drip line. Besides ^{45}Fe, the ground-state of ^{48}Ni has also been found to be of this nature.

The short-lived ground state of ^{6}Be has been known to decay by the emission of two protons since 1958. The levels associated with its decay are illustrated in Fig. 21. In this case, single-proton decay is energetically possible through the low-energy tail of the very wide ^{5}Li ground-state resonance. However, if one imagined a sequential two-proton decay passing through this ^{5}Li resonance, its lifetime is so short that the first emitted proton will have hardly moved before the second proton from the decay of ^{5}Li is released. Such a situation cannot be considered sequential and it is better to consider this decay as a prompt two-proton emission. Indeed, it was found that the angular correlations between the two emitted protons cannot be reconciled with the distribution expected if the decay passed through an intermediate state with the ^{5}Li ground-state spin of J^π=3/2$^-$ [6].

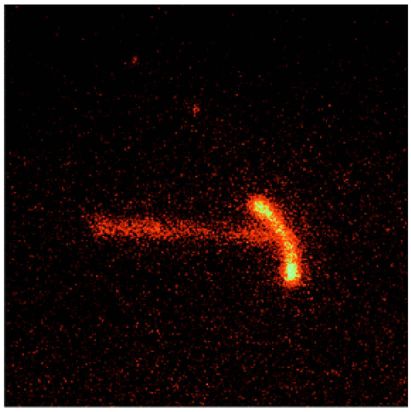

Fig. 20. A two-proton decay event recorded by an optical time projection chamber. The longer track is the ionization trail of a ^{45}Fe nucleus coming in from the left that is slowing down in a gas volume and eventually stops. The two smaller tracks originating from the end of the ^{45}Fe trail are the two-proton decay products. These protons have low energy and are stopped in the gas volume a short distance from where the ^{45}Fe decayed. Figure from Ref. [13].

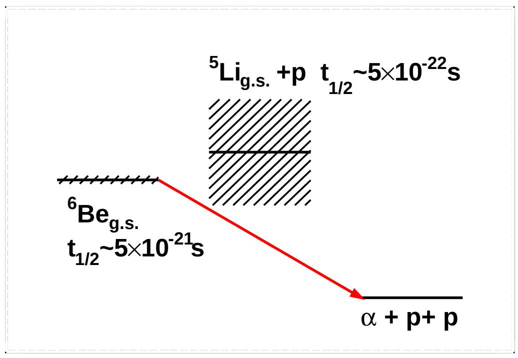

Fig. 21. Schematic showing the levels important for the decay of ^{6}Be.

Two-proton decays where the prospective intermediate is very wide and larger than the prospective decay energy of the first emitted proton are call democratic [3]. The nucleus ^{6}Be maybe considered partly of the Goldansky type as most of the strength of the ^{5}Li is energetically inaccessible and also of the democratic type as the ^{5}Li decay width is so large.

The pairing interaction is also important for the democratic decay as it causes a staggering in ground-state decay widths of odd and even-Z nuclei (odd-Z ground-states tend to have larger widths than their even-Z neighbors).

Democratic two-proton emitters are confined to light nuclei where the low Coulomb barriers permit wide odd-Z ground states. There is no experimental signatures which differentiates between the Goldansky and democratic decay modes and both can be treated using the same theoretical models.

5.3 Survey of single and two nucleon decay beyond the drip lines

The pairing interaction is important in both the Goldansky and democratic processes and thus all prompt two-proton ground-state emitters are even-Z. From a similar logic, all prompt two-neutron emitters are located in the even-N isotopes beyond the neutron drip line. Figure 22 shows a portion of the chart of nuclides summarizing the decay modes of light nuclei beyond the drip lines. Known two-proton emitters in this region (^{6}Be, ^{8}C, ^{12}O, ^{15}Ne, ^{16}Ne, and ^{19}Mg) all have even-Z. In contrast the odd-Z isotopes beyond the proton drip line are all single-proton emitters. On the neutron rich-side, we see known two-neutron ground-state emitters (^{5}H, ^{10}He, ^{13}Li, ^{16}Be, and ^{16}O) all have even N. Again the odd-N isotopes beyond the neutron drip lines are all single-neutron emitters. A number of such cases are considered virtual states, i.e., strong neutron single-particle structure but where the unbound neutron is in an ℓ=0 single-particle level and thus has no barrier. Virtual states are not true resonances, they do not show a phase shift of π radians, nor do they have a lifetime associated with them. However, if the neutron mean-field potential was made slightly deeper, then they would have a bound $s_{1/2}$ neutron level. This attractive mean field potential gives rise to attractive final-state interactions between the neutrons and the core which can often be seen as enhancements in the invariant-mass spectrum at very small core-neutron relative energies. Virtual ground-states have been reported for ^{9}He, ^{10}Li, ^{12}Li, ^{13}Be, and ^{18}B, although some of these claims have been disputed.

The lifetime of two-nucleon emitters depends on the height of the barrier constraining the two valence nucleons inside of the nucleus. Ground-state two-proton emitters show a general increase in their liftime with mass due to the increasing Coulomb barrier. The lightest two-proton emitter ^{6}Be has a lifetime of $5{\times}10{-}21$ s,^{19}Mg has a value of $\sim$4 ps [8], and as we have seen ^{45}Fe has a lifetime of $\sim$2 ns. Heavier two-proton emitter would have even larger lifetimes.

Two-neutron emitters, which have only centrifugal barriers, are generally expected to have short lifetimes. However, an exception to this is the two-neutron emitter ^{26}O which has a measured lifetime of $\sim$4.5 ps [12,10]. Such a relatively long lifetime is unexpected in a two-neutron emitter as the neutrons are only constrained by a centrifugal barrier. However, the barrier penetration probability is dependent both on the barrier height and the energy of the state inside of the barrier. Grigorenko *et al.* [9] showed, in their model calculations, that the decay energy of this state needs to be very small, less than 1 keV to attain such a long lifetime.

5.4 Heavier isotopes

The neutron drip line is known up to oxygen at present, so there is no more information on the neutron decay of heavier neutron-rich ground-state nuclei. On the other hand, partial information on the proton drip line is known up to bismuth. For example, Fig. 23 shows a portion of the chart of nuclides centered on the proton-rich Tm isotopes (Z=68). Where the proton drip line is known experimentally, it is indicated by the solid lines in this figure. The extent of the drip line for the even-Z isotopes has not been measured, but the predictions of a particular mass model are indicated by the dashed lines. The drip line has a very strong odd-even structure due to the pairing interaction creating long "fingers". Only odd-Z nuclei are known beyond the drip line at present in this region and no two-proton ground-state emitters have been identified in this region, just single-proton emitters. However predicted two-proton emitters are indicated by the yellow squares, a long way from the drip line. Now the isotopes where a one-proton branch has been identified are indicated by the green squares. Notice that odd-Z isotopes just beyond the drip line have no known proton decay branch. For example it is not until ^{147}Tm, that a ground-state proton decay branch has been identified and here it has just a 15% branching ratio with the weak decays, β^{+} and electron capture, comprising the rest of the strength. It is of the course the large Coulomb barriers that has suppressed proton decay in this region, and its not until one is well beyond the drip line that proton decay becomes significant and competes with the weak-decay modes. With the large Coulomb barriers, the lifetimes in this region are very long of order of seconds.

5.5 Correlations in two-nucleon decay

The correlations between the momentum vectors of the decay products in three-body decay contains potential information on the decay path and structure of the resonance. The three decay products, each with their own momentum vector, represents nine degrees of freedom. However in frame of the decaying system, their total momentum is zero reducing the degrees of freedom to six. As the sum of the kinetic energies of the products is fixed to the decay energy, this also reduces the degrees of freedom by one to five. Finally, any orientation of the momentum vectors can be randomly rotated by the three Euler angles. These orientations are all considered equivalent, so this leaves us with two final degrees of freedom to fully describe the momentum correlations. So for three-body decay, the correlations between the momenta of the three decay products can be represented by a two-dimensional distribution. One has a choice in the exact variables for the two axes.

We will concentrate on only one aspect of these correlations concerning the kinetic energy sharing between

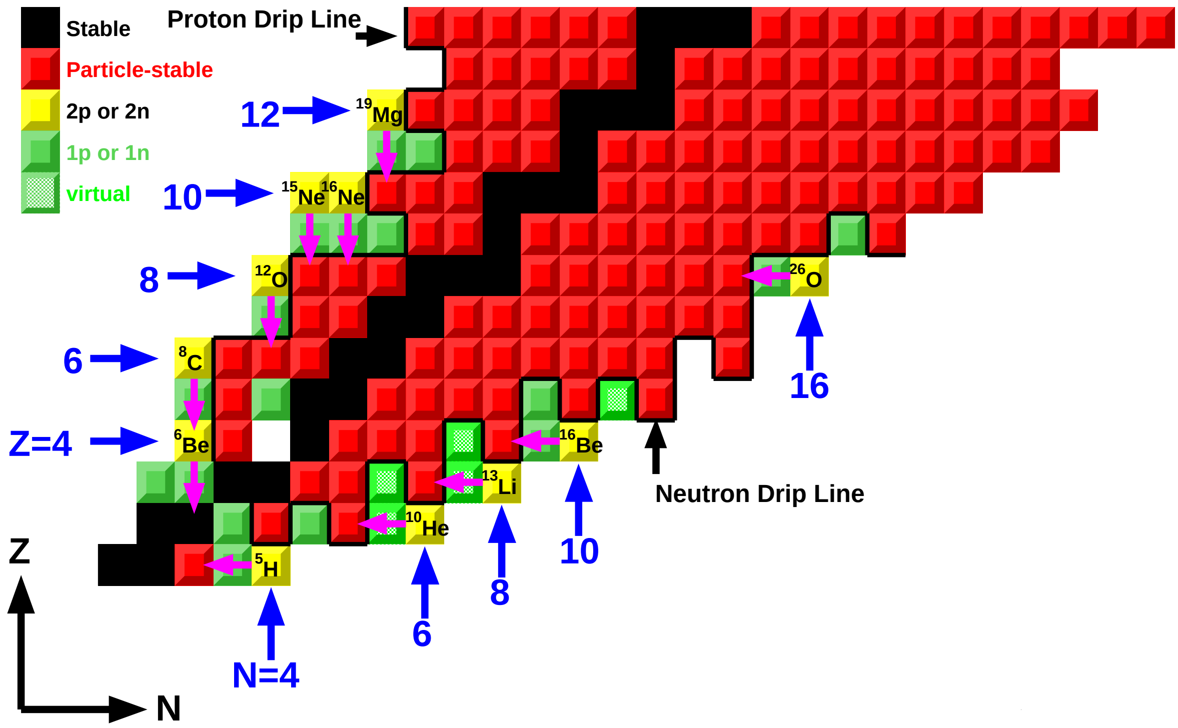

Fig. 22. A portion of the chart of nuclides for light isotopes showing the ground-state decay modes and the drip lines.

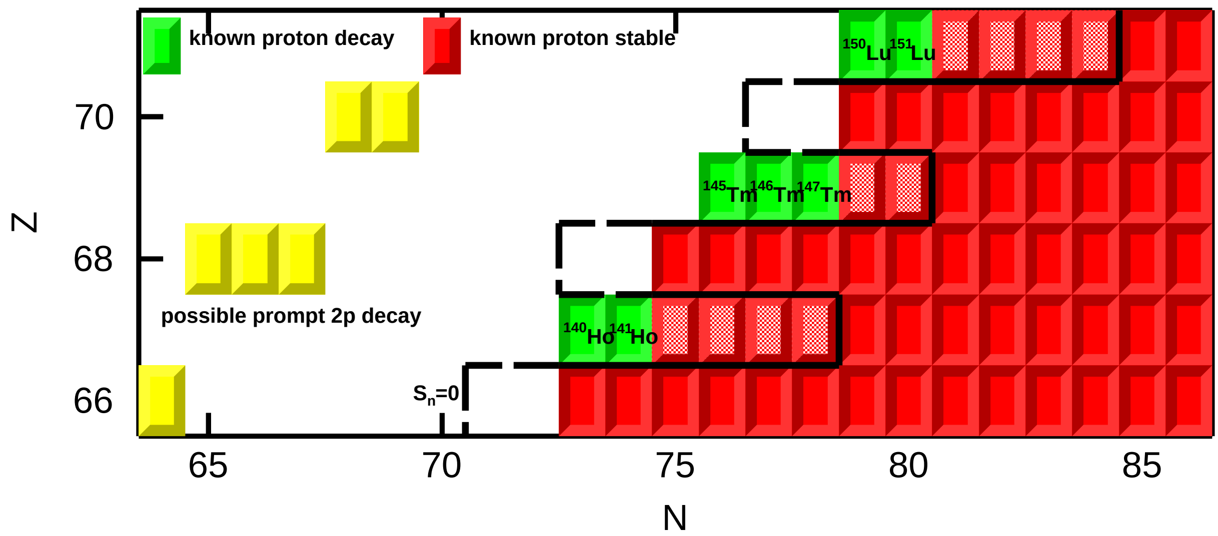

Fig. 23. A portion of the chart of nuclides for heavier isotopes showing the ground-state decay modes and the proton drip line. The proton drip line is only known experimentally for the odd-Z elements (solid black line). For the even-Z istopes the location of the drip line (dash black line) is estimated from a mass model. The predicted location of two-proton emitters from Ref. [15] is also shown.

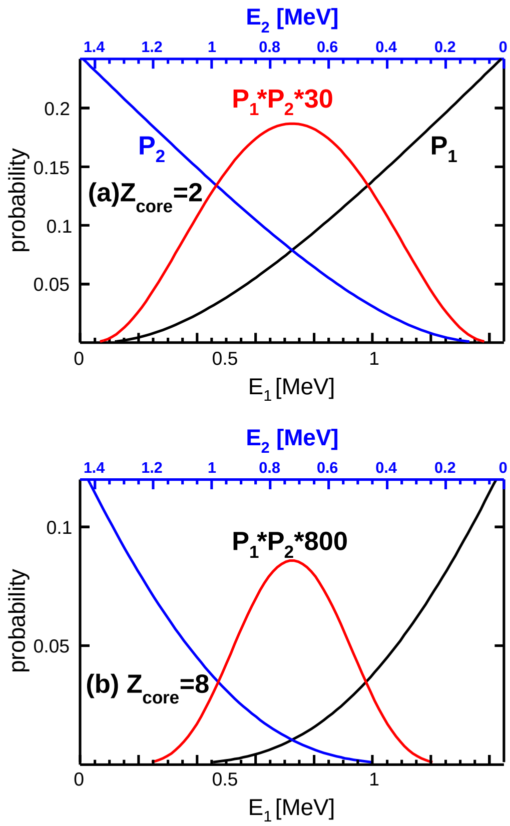

Fig. 24. Kinetic energies in two-proton decay. Dependence of the barrier penetration probabilities of the two protons (P_1 and P_2) and their product on the energies of the two protons E_1 and E_2. Results are shown for a total decay energy of E_1+E_2=1.45 MeV and (a) a core of Z_{core}=2 and (b) a core of Z_{core}=8.

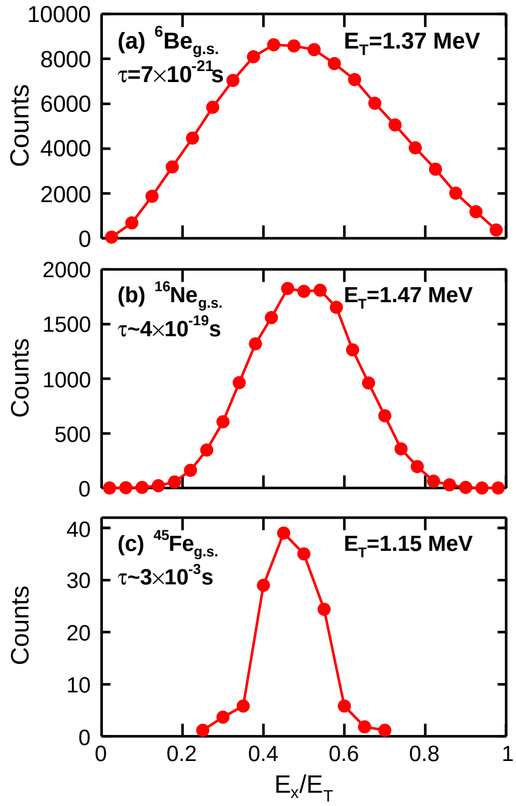

Fig. 25. Experimental distributions of the relative kinetic energy between one of the protons and the core for three ground-state two-proton emitters.

the two protons. Consider the case of a large core mass where the core kinetic energy in the center-of-mass frame is small. If the kinetic energies of the two protons are E_1 and E_2 where $E_1 + E_2 = E_T$ (the total decay energy) which is a constant, then the distribution $f(E_1)$ of the kinetic energies can be obtained from the product of the barrier penetration probabilities, i.e,

$$f(E_1) \propto P(E_1)P(E_2). \tag{36}$$

Figure 24 shows the kinetic energy dependence of the two barrier penetrating factors and their products for a total decay energy of 1.45 MeV and for cores of Z_{core}=2 and 8. The product of the two terms always peaks at E_1=E_2=$E_T/2$ and the more sub-barrier the penetration, the faster the penetration factors increase with kinetic energy, and thus the narrower is the maximum in the product. This argument was originally made by Goldansky to conclude that, on average, the two protons have equal kinetic energies in two-proton decay. As the Coulomb barrier becomes larger for heavier masses and the two-proton decay becomes more sub-barrier, the fluctuations around equal energy sharing also becomes smaller. Experimentally this trend has been established. Figure 25 shows the measured distributions of E_x/E_T where E_x can be either E_1 or E_2, i.e., relative kinetic energy between one of the protons and the core for three ground-state two-proton emitters. All measured distributions peak close to 0.5, i.e., where the two proton kinetic energies are equal. Also the widths of these experimental distributions become narrower with increasing mass number reflecting the larger Coulomb barriers.

6 Compound Nucleus Decay

So far we have concentrated on ground-state resonances and those at low excitation energies. As the excitation energy increases, the spacing between resonances D get smaller i.e., the level density increases, and the average width of the resonances increases. At some point we leave the region of isolated resonances where they are separated from each other and start the region of overlapping resonances (as displayed schematically in Fig. 26) where concept of a compound nucleus comes into play.

6.1 Level Density

In order to estimate how quickly the level density increases with excitation energy, we can start with our simple single-particle model. Let us just consider one type of nucleon

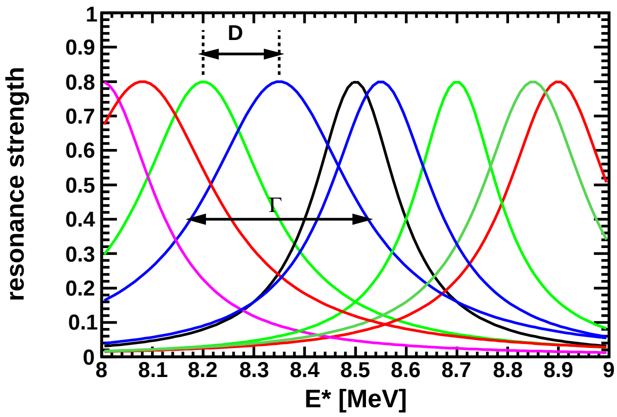

Fig. 26. Schematic showing the lines shapes of overlapping resonances in the start of the compound-nuclei region. Here Γ is the typical width of a resonance while D is the typical energy separation between neighboring resonances.

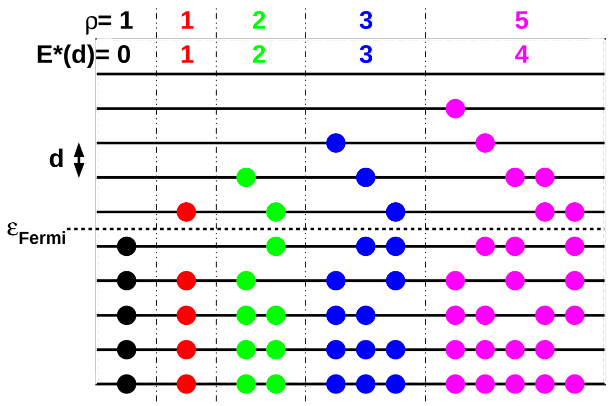

Fig. 27. Enumeration of single-particle configurations for the specified excitation energies for a model of equally spaced single-particle levels.

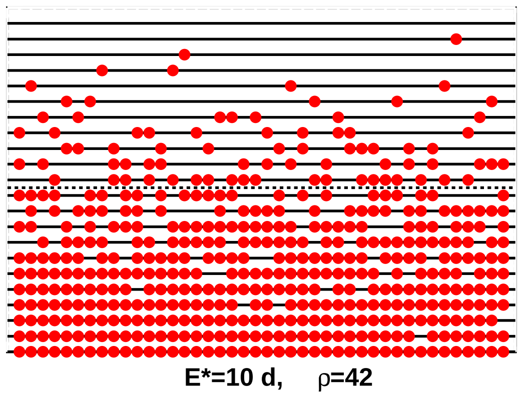

Fig. 28. Enumeration of the single-particle configurations for an excitation energy of 10 d, where d is the spacing between single-paricle levels.

and ignore the nucleon spin. For further simplification, let us assume the single-particle levels have uniform spacing, separated by an energy d. As different nuclear states are produced by rearranging the filling of the single-particle levels, it is clear that only excitation energies of multiples of d are allowed in this model. Figure 27 enumerates the possible single-particle configurations that produce the ground state and excitation energies of d, $2d$, and $3d$ in this model. In this figure, dots are a filled levels and each vertical row of dots represents a different single-particle configuration.

The ground state is a single configuration where all the level are filled up to the Fermi energy ε_{Fermi}. The first excited state ($E^* = d$) is obtained by promoting the valence nucleon to the next higher single-particle state creating a particle-hole excitation. There are two ways of obtaining $E^* = 2d$; either promoting the valence nucleon up two single-particle levels or promoting the nucleon below this valence level by two units of d. In both case one is making a particle-hole excitation. There are three ways of producing excitation energy $E^* = 3d$, again all involve particle-hole excitations. There are five ways of producing $E^* = 4d$, either by a single particle-hole excitations or by a two-particle-two-hole excitation. Higher excitation energies require one to consider all the possible combinatorics of particle-hole and multi-particle, multi-hole excitations. Although for the low excitation energies considered in Fig. 27, the level density did not increase drastically, this behavior changes. For $E^* = 10d$, there are 42 possible combinations, which are displayed in Fig. 28, and the combinatorics increase very rapidly at even higher excitation energies.

Analytical solutions to this problems were first consider by Euler 1737, though not in terms of nuclear levels densities. The nuclear problem was solved by Bethe in 1936 and the solution is called the Fermi-gas level density, i.e.,

$$\rho(E^*) = \frac{1}{\sqrt{48}E^*} \exp\left(2\sqrt{aE^*}\right), \tag{37}$$

where the level-density parameter is

$$a = \frac{\pi^2}{6} g \tag{38}$$

and g is the single-particle level density. In our simple model $g = 1/d$, but the formula can be extended to include realistic ingrediants including two nucleon types and nonequal single-particle spacings where now

$$a = \frac{\pi^2}{6} \left[g_n(\varepsilon^n_{Fermi}) + g_p(\varepsilon^p_{Fermi})\right] \tag{39}$$

which includes the sum of the neutron and proton single-particle level densities at their respective Fermi energies. Of course our single-particle picture has deficiencies as discussed in Sec. 3. Although configuration mixing conserves the number of nuclear levels, there is some rearrangement in their energies. Modifications have been made

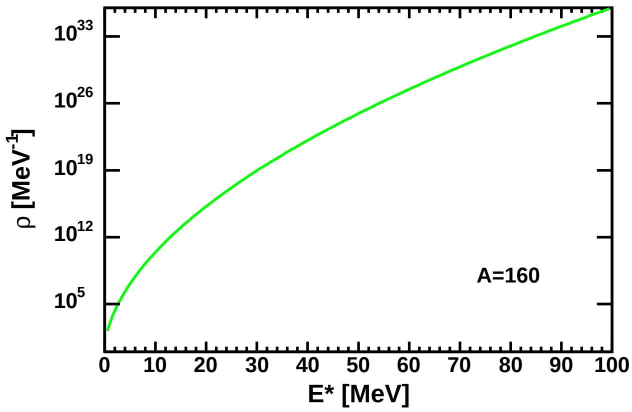

Fig. 29. Nuclear level density in the Fermi-gas model as a function of excitation energy for A=160.

to the Fermi gas formula to account for these effects, but these modifications wash out with excitation energy and the Fermi gas form is generally consider to be the correct asymptotic form at high excitation energies.

Using realistic single-particle level densities, we show the nuclear level density obtain from Eq. (37) for a nucleus with A=160 in Fig. 29. For nuclei near stability, the neutron separation energy is around 8 MeV. The resonances start above this separation energy. From Fig. 29 we see that there are $\sim 10^9$ level per MeV at E^*=8 MeV. This is quite different to the lighter nuclei we considered in the beginning of this work. For example, consider the neutron resonances in ^{13}C shown Fig. 8. The first resonance does not occur until $\sim$2 MeV above the n+^{12}C threshold. This demonstrates the strong dependence of the nuclear level density on mass number A.

Obviously with such large nuclear level densities in the resonance region for these heavier nuclei, it is impossible to determine the level density by counting all of these levels. However for neutron energies just above the neutron threshold, one only sees resonances with ℓ=0 in elastic scattering and total cross section measurements. For example, the total cross section measured for n+^{232}Th at energies up to 200 keV is shown in Fig. 30. At these small energies, the barrier penetration probabilities P_ℓ are very small for $\ell > 0$. For example at E_n=100 keV, P_0=1 while $P_1 \sim 10^{-4}$ and with similar Θ^2 values, the $\ell = 1$ resonances with be greatly suppressed. Thus the peaks observed in Fig. 30 are all $s_{1/2}$ resonances associated with J=1/2$^+$ states in ^{233}Th.

From measurements such as these, the density of $s_{1/2}$ levels has been obtained for most stable isotopes. The Fermi-gas formula can been extended to give the density

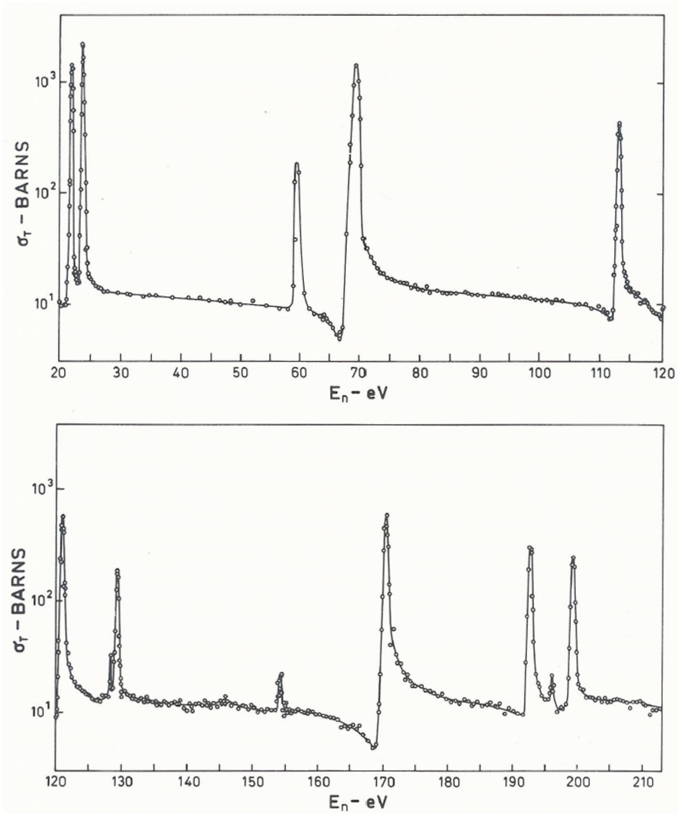

Fig. 30. Total neutron cross section for the reaction n+^{232}Th for neutron energies up to 210 keV. Taken from Ref. [4].

of levels for a fixed J, i.e.

$$\rho(E^*, J) \propto a^{5/2} \frac{2J+1}{(E^* - \frac{J(J+1)}{2\mathcal{I}_{rig}})^{7/4}} \times \exp\left[2\sqrt{a\left(E^* - \frac{J(J+1)}{2\mathcal{I}_{rig}}\right)}\right] \quad (40)$$

where $\mathcal{I}_{rig}$ is an rigid-body moment of inertia of the nucleus. Using this formula, the level-density parameter can be extracted from the density of $s_{1/2}$ levels. The mass dependence of extracted level-density parameters [2] is shown in Fig. 31.

These experimental level-density parameters approximately follow the linear relationship, $a = A/8$ MeV^{-1}, but there are large fluctuations associated with shell closures which is most noticeable at A=208, corresponding to region near the double closed-shell nucleus ^{208}Pb. Shell closures correspond to large gaps between the single-particle levels, and hence to small level-density parameters a. These neutron-resonance measurements cannot be extended to unstable nuclei so the symmetry $[(N-Z)/A]$ dependence of the level-density parameter is not well established.

6.2 Decay in the Overlap region

In region of excitation energies with high level densities, there are many single-particle configurations of similar en-

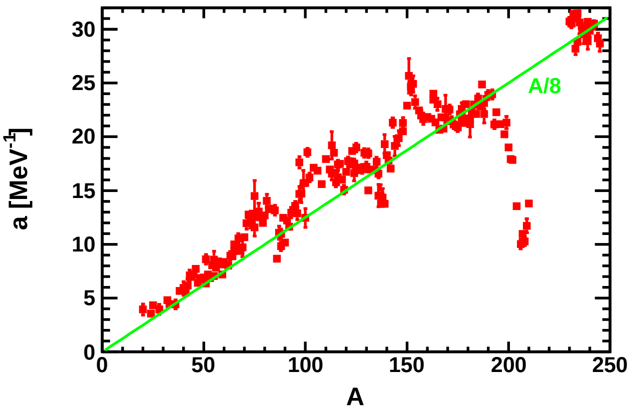

Fig. 31. Level-density parameters extracted from the density of ℓ=0 neutron resonances just above the neutron separation energy.

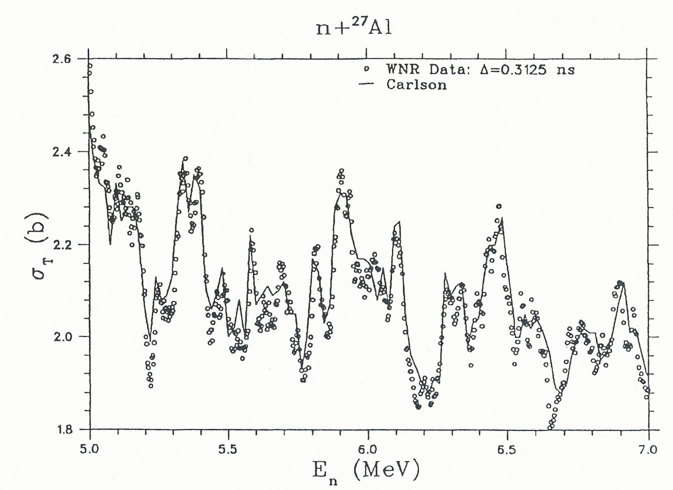

Fig. 32. Eriscon fluctuations in the total cross section for n+^{27}Al reaction from Re. [14].

ergy for which one can mix. Thus configuration mixing is especially strong in this region and levels generally do not have strong single-particle character. Also with this strong mixing, the decay of a resonance can be spread over many exit channels.

When we first enter the region of overlapping levels, the cross section for any open channel show strong fluctuations. For example in Fig. 32, the total cross section for the n+^{27}Al reaction at neutron energies of 5 to 7 MeV is shown. The fluctuations are not individual resonances, rather they are due to interferences between the overlapping resonances in ^{28}Al. These fluctuations were originally predicted by Ericson in 1960 [5] and they are over energy scales of the order of the mean decay width. Given the large number of resonances involved, one cannot contemplate predicting the details of these fluctuations. Rather the mean values of the cross section after the fluctuations have been smoothed out are amenable to prediction. Such smoothing is often done experimentally due to the experimental energy resolution. Also in the limit of extreme mixing, the fluctuation-averaged partial widths can be obtained from statistical arguments giving rise to the statistical model of compound-nucleus decay

6.3 Particle Evaporation

In the statistical model, the total decay width for neutron or charged particle emission in the overlap region is determined using the prescription developed separately by Weisskopf and Ewing using the principle of detail balance. Consider a compound nucleus with excitation energy E^* at rest in a confining box of volume V with elastic walls which is shown as state (a) in Fig. 33. If the compound nucleus decays emitting a neutron with kinetic energy from E_k to $E_k + dE$ (velocity v and momentum p) then it is in state (b) of Fig. 33. By energy conservation, the daughter nucleus formed after the neutron emission will have an excitation energy of $E^* - S_n - E_k$.

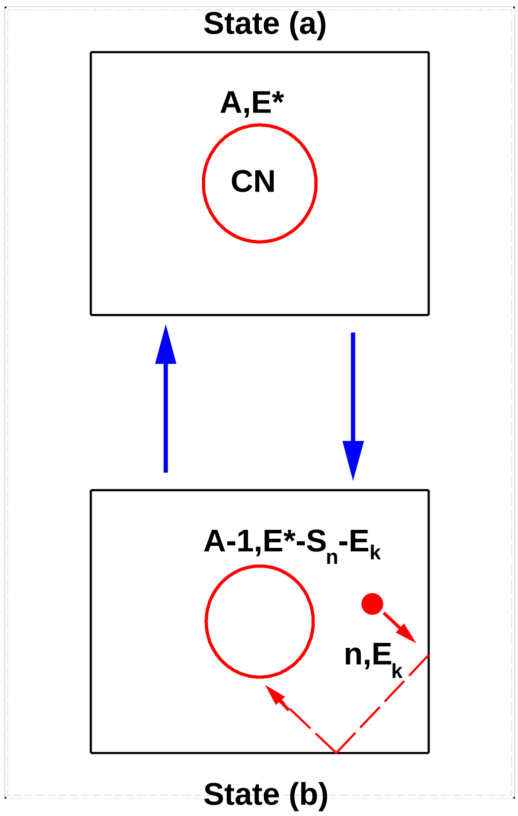

Fig. 33. Schematic showing the equilibrium between the emission and absorption of a neutron for an compound nucleus enclosed in a reflecting box.

The neutron can bounce around the box elastically until it is eventually reabsorbed into the compound nucleus. If we consider an equilibrium is achieved between states (a) and (b), then from the principle of detail balance

$$\rho_a w_{ab} = \rho_b w_{ba} \tag{41}$$

where ρ_a and ρ_b are the density of states for configurations (a) and (b), respectively and w_{ab} is the rate of transition from (a) to (b), while w_{ba} is the reverse rate.

Now ρ_a is just the compound-nucleus level density $\rho_{CN}(E^*)$ while ρ_b consists of the product of the phase space of the neutron $4\pi p^2 V/\hbar^3 dp/dE_k dE_k$, the neutron's spin multiplicity $2s+1$ where s=1/2 for a neutron, and the level density of the daughter $\rho_d(E^*-S_n-E_k)$. Thus

$$\rho_b = (2s+1)\frac{4\pi p^2 V}{\hbar^3}\rho_d(E^*-S_n-E_k). \tag{42}$$

The reverse rate w_{ba} is related to the cross section $\sigma_{inv}(E_k)$ for capture of the neutron by the daughter. This is often called the inverse capture cross section in this context. This cross section represents the effective area around the neutron for which interactions with the target can occurs. In unit time, this area sweeps out a volume $v\sigma_{inv}$ and the probability of interacting with the daughter nucleus is then just the ratio of this volume to the total box volume, i.e.,

$$w_{ba} = \frac{v\sigma_{inv}(E_k)}{V}. \tag{43}$$

We can thus solve Eq. (41) to obtain the forward rate which is related to the patial decay width, i.e.,

$$w_{ab} = \frac{\Gamma_n(E_k)dE}{\hbar} = \frac{(2s+1)m}{(\pi\hbar)^2}E_k\sigma_{inv}(E_k) \times \frac{\rho_d(E^*-S_n-E_k)}{\rho_{CN}(E^*)} \tag{44}$$

Notice that the box volume V has dropped out of this equation and thus we are at liberty to increase the box size to infinity. The assumption in statisical theory is that this equilibrium rate w_{ab} is still valid even when the reverse process is absent.

Integrating over all neutron energies we obtain the total partial decay width for neutron emission as

$$\Gamma_n(E^*) = \frac{(2s+1)m}{(\pi\hbar)^2\rho_{CN}(E^*)} \times \int_0^{E^*-S_n} E_k\sigma_{inv}\rho_d(E^*-S_n-E_k)dE. \tag{45}$$

Similar expressions can be derived using detailed balance for proton, α-particle, and γ emissions and the sum of these represents the total decay width Γ_{tot}. Again the probability for neutron emission is just Γ_n/Γ_{tot}.

The many possible decay channels for a compound nucleus are illustrated by the schematic in Fig. 34. We show only proton and neutron decay modes here, but α-particle and more complex fragments can be emitted. For heavy nuclei, fission decay can also be incorporated as a competing mode. The figure differentiates decays to the regions of isolated and overlapping resonances in the daughter nuclei. If the decay is to the overlapping resonance region, then this daughter should be considered as a compound nucleus itself and its decay modes can be similarly enumerated. By such a mechanism, a initial compound nucleus can decay by a series of sequential particle or γ decays as it loses its initial excitation energy eventually arriving at a ground-state.

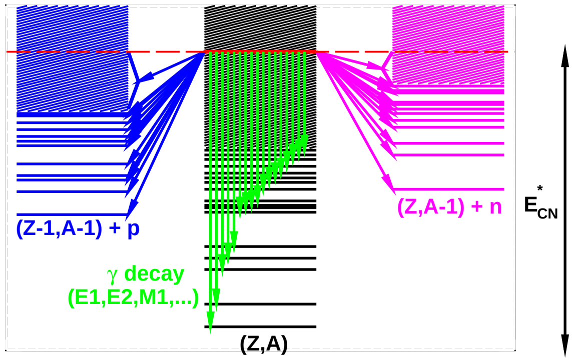

Fig. 34. Schematic illustrating the varied possible decay paths of a compound nucleus. For both the initial and possible daughter nuclei, the decay can be to the region of isolated levels or to the region of overlapping levels (hashed regions).

6.4 Fusion Reactions for Creating Proton-Rich Nuclei

As an example of compound-nucleus decay, consider the creation of the ground-state proton emitters in Tm isotopes of Fig. 23. These isotopes were produced with fusion-evaporation reactions. The ^{147}Tm isotope was produced via the E=261 MeV ^{58}Ni+^{92}Mo fusion reaction producing a ^{150}Yb compound nucleus with an excitation energy of E^*=52 MeV. This excitation energy is removed by a sequential series of mainly proton emissions, but α and neutron emissions can contribute. The emission of γ- rays does not becomes significant until particle emission is energetically forbidden. Three examples of the possible decay sequences are listed as Eqs. (46-48).

In the first case [Eq. (46)], three protons are emitted sequentially forming a ^{147}Ho excited state which then γ decays to its ground state. In the second example [Eq. (47)], the first two steps are the same as in the first case, but a neutron is emitted at the third step. In the third example [Eq. (48)], neutrons are emitted in the first and the third steps. In addition to these examples, many other decay sequences are possible. Such decay processes are very amenable to Monte Carlo techniques. The probabilities at each possible decay step are calculated for each compound nucleus and the decay mode is chosen from these

$$^{150}\mathrm{Yb}^* \rightarrow^{149} \mathrm{Tm}^* + p \rightarrow^{147} \mathrm{Er}^* + p + p \rightarrow^{147} \mathrm{Ho}^* + p + p + p \rightarrow^{147} \mathrm{Ho}_{g.s.} + p + p + p + \gamma\text{'s} \quad (46)$$

$$^{150}\mathrm{Yb}^* \rightarrow^{149} \mathrm{Tm}^* + p \rightarrow^{148} \mathrm{Er}^* + p + p \rightarrow^{147} \mathrm{Er}^* + n + p + p \rightarrow^{147} \mathrm{Er}_{g.s.} + p + p + n + \gamma\text{'s} \quad (47)$$

$$^{150}\mathrm{Yb}^* \rightarrow^{149} \mathrm{Yb}^* + n \rightarrow^{148} \mathrm{Tm}^* + p + n \rightarrow^{147} \mathrm{Tm} + n + p + n \rightarrow^{147} \mathrm{Tm}_{g.s.} + n + p + n + \gamma\text{'s} \quad (48)$$

probabilities in a Monte Carlo fashion. If the new daughter nucleus is excited, then the probabilities for its possible decay modes are calculated and again the decay path is chosen in a Monte Carlo fashion. This is continued until the excitation energy is exhausted.

The distribution of final products, called evaporation residues, predicted by a Monte Carlo code is shown in Fig. 35. The relative yield for each isotopes is indicated by the area of the black circles. The highest yield are predicted to be for ^{147}Ho and ^{146}Dy isotopes corresponding to the emission of three and four protons respectively. The nuclei in this region are all proton-rich with small proton separation energies making proton emission more probable than neutron emission. The other significant residues populated are ^{147}Er and ^{146}Ho corresponding to the $2pn$ and $3pn$ channels and ^{144}Dy formed from the $\alpha 2p$ channel. The yield for the ground-state emitter ^{147}Tm from the $p2n$ chanel is quite small, it is predicted to represent less than 1% of the total yield.

The discovery of the lighter two Tm isotopes (^{145}Tm and ^{144}Tm) was achieved with the same fusion reaction, but with higher bombarding energies and hence with compound nuclei of higher excitation energies. This increased excitation energy permitted the evaporation of more particles in the decay allowing for the small probability of emitting extra neutrons to form these more proton-rich Tm isotopes.

6.5 Compound-nucleus decay in the r-process

Another example of the use of the statistical model of compound-nucleus decay is for r-process nucleosynthesis. This process is thought to occur in astrophysical environments with large neutron fluxes. Initial seed nuclei can begin a series of neutron capture and β decays creating neutron-rich isotopes close to the neutron drip line all the way up to uranium. After the astrophysical event creating the neutron flux dies down, the neutron-rich isotopes created in this process undergoe a series β decays eventually producing the stable isotopes.

In modeling this process and determining which astrophysical events (supernova or neutron-star merges) are the main contributer to r-process material, it is necessary to know the neutron capture cross sections. The capture can be through a resonance where the cross section is given by the product of two terms, i.e., $\sigma_{capture}$ and $\Gamma_\gamma/\Gamma_{tot}$. The first term, the capture cross section, gives the probability that a resonance is formed while the second gives the probability that it decays by γ emission rather than re-emitting the captured neutron. In some cases we are dealing with capture by an isolated resonance, in which case detailed knowledge of the resonance parameters are needed. Alternatively the capture could be to the overlapping region and here the statistical model can be used to determined the second term. One of the greatest uncertainties in this case, is the knowledge of the level-density parameters for such neutron-rich isotopes. The neutron-resonance-counting method that was used to obtained the systematics of Fig. 31 can only work for stable isotopes. Clearly knowledge of the locations of closed-shells is required for the neutron-rich system, but it is important to know if the average behavior still follows the $A/8$ MeV^{-1} dependence seen in Fig. 31 or are there important dependences on the asymmetry parameter $(N-Z)/A$ not considered. These topics are under active research at the present moment.

7 Conclusions

In the preceding sections we have investigated the diverse nature of resonances. Although the basic features of resonances can be understood in a purely single-particle picture where barrier penetration gives rise to the long lifetimes, this picture does not apply to all resonances. However this single-particle picture can provide an a reasonable approximation for some lower-lying resonances. But for other lower-lying resonances and those at higher excitations, mixing of these single-particle configuration is very important. This mixing becomes quite extreme in the region of overlapping resonances at higher excitation energies.

Beyond the drip lines, all ground states are resonances and giving rise to ground-state neutron and proton emitters. The ground-state proton emitters tend to have longer lifetimes than their neutron emitting cousins due to the presence of their Coulomb barriers which retards their decay. This trend is most pronounced for heavier nuclei beyond the proton drip line where the larger Coulomb barriers give rise to proton lifetimes which are of similar order or smaller than weak decay lifetimes.

In addition to ground states which decay by single nucleon emission, the pairing interaction is responsible for the existence of two-proton and two-neutron emitters. Such ground-state nuclei undergo a novel three-body decay mechanism.

At high excitation energies, resonances start to overlap. In this regime, the concept of a compound nucleus was explored. Compound nuclei can decay by a series of proton, neutron, α-particle emissions creating a distribution of ground-state isotopes. Such reactions have been

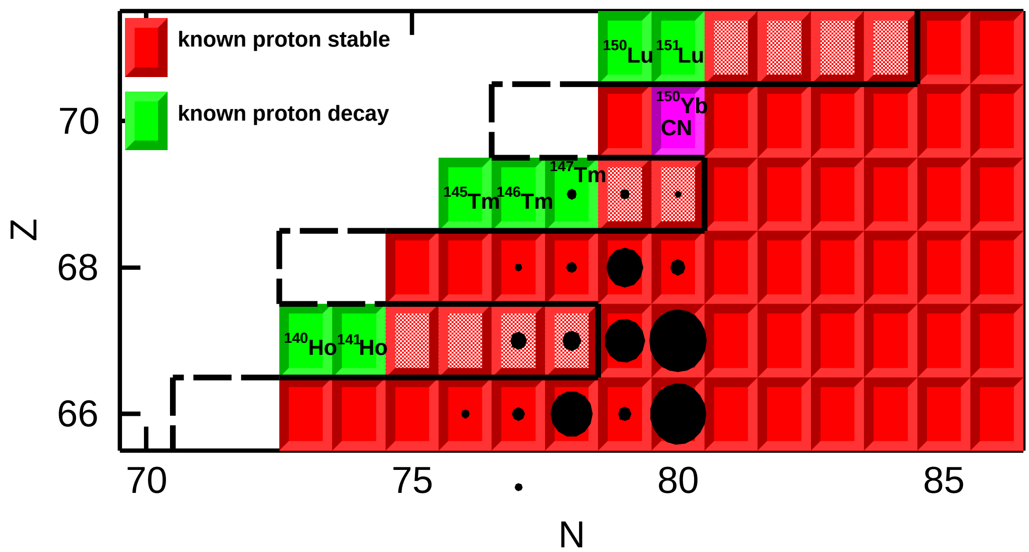

Fig. 35. Predicted yield of final decay products following the decay of the compound nucleus ^{150}Yb with 52 MeV of excitation energy. The yield of a particular nuclide is proportional to the area of circle. A small fraction of the yield is in isotopes beyond the proton drip line which permits one to study their ground-state proton decay.

used to create the heaviest ground-state proton emitters identified. The compound-nucleus decay of very neutron exotic nuclei ia also important for understanding the r-process in nucleosynthesis. Clearly resonances are vibrant area of research for exotic nuclei and will continue to be so in the future.

References

1. G. Aad et al. *Phys. Rev. D*, 90:052004, Sep 2014.
2. H. Baba. *Nucl. Phys. A*, 159:625, 1970.
3. O.V. Bochkarev, L.V. Chulkov, A.A. Korsheninniicov, E.A. Kuz'min, I.G. Mukha, and G.B. Yankov. Democratic decay of 6be states. *Nuclear Physics A*, 505(2):215 – 240, 1989.
4. A. Bohr and B. R. Mottleson. *Nuclear Structure*, volume I. Benjamin, New York, 1969.
5. Torleif Ericson. Fluctuations of nuclear cross sections in the "continuum" region. *Phys. Rev. Lett.*, 5:430–431, Nov 1960.
6. D. F. Geesaman, R. L. McGrath, P. M. S. Lesser, P. P. Urone, and B. VerWest. Particle decay of ^{6}Be. *Phys. Rev. C*, 15:1835–1838, May 1977.
7. V.Z. Goldberg, B.T. Roeder, G.V. Rogachev, G.G. Chubarian, E.D. Johnson, C. Fu, A.A. Alharbi, M.L. Avila, A. Banu, M. McCleskey, J.P. Mitchell, E. Simmons, G. Tabacaru, L. Trache, and R.E. Tribble. First observation of 14f. *Physics Letters B*, 692(5):307 – 311, 2010.
8. L. V. Grigorenko, I. G. Mukha, and M. V. Zhukov. Lifetime and fragment correlations for the two-neutron decay of ^{26}**O** ground state. *Phys. Rev. Lett.*, 111:042501, Jul 2013.
9. L. V. Grigorenko, I. G. Mukha, and M. V. Zhukov. Lifetime and fragment correlations for the two-neutron decay of ^{26}**O** ground state. *Phys. Rev. Lett.*, 111:042501, Jul 2013.
10. Z. Kohley, T. Baumann, D. Bazin, G. Christian, P. A. DeYoung, J. E. Finck, N. Frank, M. Jones, E. Lunderberg, B. Luther, S. Mosby, T. Nagi, J. K. Smith, J. Snyder, A. Spyrou, and M. Thoennessen. Study of two-neutron radioactivity in the decay of ^{26}**O**. *Phys. Rev. Lett.*, 110:152501, Apr 2013.
11. A. M. Lane and R. G. Thomas. R-matrix theory of nuclear reactions. *Rev. Mod. Phys.*, 30:257–353, Apr 1958.
12. E. Lunderberg, P. A. DeYoung, Z. Kohley, H. Attanayake, T. Baumann, D. Bazin, G. Christian, D. Divaratne, S. M. Grimes, A. Haagsma, J. E. Finck, N. Frank, B. Luther, S. Mosby, T. Nagi, G. F. Peaslee, A. Schiller, J. Snyder, A. Spyrou, M. J. Strongman, and M. Thoennessen. Evidence for the ground-state resonance of ^{26}**O**. *Phys. Rev. Lett.*, 108:142503, Apr 2012.
13. K. Miernik, W. Dominik, Z. Janas, M. Pfützner, L. Grigorenko, C. R. Bingham, H. Czyrkowski, M. Ćwiok, I. G. Darby, R. Dabrowski, T. Ginter, R. Grzywacz, M. Karny, A. Korgul, W. Kuśmierz, S. N. Liddick, M. Rajabali, K. Rykaczewski, and A. Stolz. Two-proton correlations in the decay of ^{45}Fe. *Phys. Rev. Lett.*, 99:192501, Nov 2007.
14. V. Mishra, N. Boukharouba, S. M. Grimes, K. Doctor, R. S. Pedroni, and R. C. Haight. Determination of the level density of ^{29}Si from ericson fluctuations. *Phys. Rev. C*, 44:2419–2425, Dec 1991.
15. E. Olsen, M. Pfützner, N. Birge, M. Brown, W. Nazarewicz, and A. Perhac. Landscape of two-proton radioactivity. *Phys. Rev. Lett.*, 110:222501, May 2013.
16. M. J. Rapp, Y. Danon, F. J. Saglime, R. M. Bahran, D. G. Williams, G. Leinweber, D. P. Barry, and R. C. Block. *Nucl. Sci. Eng.*, 172:268, 2012.
17. M. S. Wallace, M. A. Famiano, M.-J. Van Goethem, A. M. Rogers, W. G. Lynch, J. Clifford, J. Lee, S. Labostov, M. Mocko, L. Morris, A. Moroni, B. E. Nett, D. J. Oostdyk, R. Krishnasamy, M. B. Tsang, R. D. de Souza, S. Hu-

dan, L. G. Sobotka, R. J. Charity, J. Elson, and G. L. Engel. *Nucl. Instrum. Methods A*, 583:302, 2007.